

Tutorial on Silicon Photonics Integrated Platform Fiber Edge Coupling

Sergey S. Avdeev^{1,2}, Aleksandr S. Baburin^{1,2}, Evgeniy V. Sergeev¹, Alexei B. Kramarenko¹, Arseniy V. Belyaev¹, Danil V. Kushnev¹, Kirill A. Buzaverov¹, Ilya A. Stepanov¹, Vladimir V. Echeistov^{1,2}, Sergey V. Bukatin¹, Ali Sh. Amiraslanov¹, Evgeniy S. Lotkov¹, Dmitriy A. Baklykov¹, and Ilya A. Rodionov^{1,2*}

¹ Shukhov Labs, Quantum Park, Bauman Moscow State Technical University, Moscow, 105005, Russia

² Dukhov Automatics Research Institute, VNIIA, Moscow 127030, Russia

*e-mail: irodionov@bmstu.ru

KEYWORDS: *silicon photonics, integrated photonics, edge coupling, coupling efficiency*

ABSTRACT: Photonic integrated circuits (PICs) play a crucial role in almost every aspect of modern life, such as data storage, telecommunications, medical diagnostics, green energy, autonomous driving, agriculture, and high-performance computing. To fully harness their benefits, an efficient coupling mechanism is required to successfully launch light into waveguides from fibers. This study introduces low-loss coupling strategies and their implementation for a silicon nitride integrated platform. Here we present an overview of coupling technologies, optimized designs, and a tutorial on manufacturing techniques for inverted tapers, which enable effective coupling for both transverse-magnetic and transverse-electric modes. The optimized coupling losses for the UHNA-7 fiber and the inverted taper Si₃N₄ coupler reached \sim -0.15 dB at 1550 nm per connection for single-mode waveguides with 220×1200 nm cross section. The measured coupling losses in the inverted taper coupler with a standard single-mode fiber were \sim -1.50 dB at 1550 nm per connection for the same platform.

INTRODUCTION

With the growing demand for high-speed and compact devices, photonic integrated circuits (PICs) are attracting significant interest because of their high bandwidth and compatibility with large-scale integration technologies. Silicon nitride (Si₃N₄) is the ideal platform for photonic integrated circuit applications such as LiDAR [1], optical sensing [2–7], bio-spectroscopy [8], communication [9] and for uses in the quantum domain, such as quantum key distribution (QKD), quantum computing [10,11] and quantum sensing [12]. In recent years, Si₃N₄ has attracted significant attention as a PIC platform because of its low propagation loss, compatibility with heterogeneous integration, extended transparent bandwidth, and lower susceptibility to errors during the lithography and etching processes compared with the silicon-on-insulator (SOI) platform [13–16]. Typically, PICs require an effective coupling mechanism to launch light into the waveguide from a fiber. To this end, grating and edge couplers are widely employed [17–43]. Grating couplers are used in out-of-plane coupling. For high-volume manufacturing by standard production techniques, for example, in MPW fabs, gratings exhibit a rather low coupling efficiency of \sim -5.0 dB and inherently suffer from limited wavelength bandwidth [17–23]. To enhance the coupling efficiency, an

inverted taper could be introduced, as it demonstrates a coupling loss of down to \sim -0.5 dB [23–26]. However, it should be noted that waveguide type and dimensions and fiber/waveguide mode size differences play a crucial role in coupling efficiency.

Edge couplers exhibit high in-plane light coupling efficiency and a broader spectral bandwidth. Most edge couplers are designed to entail long adiabatic tapers with lengths exceeding several hundred micrometers, thereby enhancing the mode transfer efficiency. Several techniques make it possible to further improve coupling efficiency, like the 2×2 couplers [29–33], mode multiplexers [20,33–35], and polarization splitters/rotators [36–43]. The compact form of the adiabatic taper drastically facilitates its applicability in high-density PICs [17]. To obtain a short and efficient taper that is applicable in high-density PICs, various taper configurations, including nonlinear, stepwise cascaded, multilayered, and metamaterials, as well as double-tip and sinusoidal taper, have been extensively analyzed for various photonic platforms [21–29]. However, unlike other platforms, compact tapers for Si₃N₄ platform edge couplers have rarely been investigated or reported. The main published results are presented in Table 1.

Table 1. Si₃N₄ taper coupling losses overview

Reference / Wavelength	Taper length / width	Coupling efficiency	3-dB alignment tolerance		Fiber type (mode size)	Waveguide crossection / technology
		TE mode, Losses	Horizontal	Vertical		
[44] Calculated 1550 nm	500 μ m / 300 nm	-0.087 dB	$\pm 3.6 \mu$ m	$\pm 3.5 \mu$ m	UHNA-3 (4.1 \pm 0.3 μ m)	100 \times 900 nm / a single step litho
[44] Measured 1550 nm		-0.17 dB	$\pm 3.8 \mu$ m	$\pm 3.6 \mu$ m	UHNA-3 (4.1 \pm 0.3 μ m)	
[45] Measured 1550 nm	500 μ m / 180 nm	-2.0 dB	-	-	LPMFs (2.5 \pm 0.3 μ m)	400 \times 700 nm / polished with diamond films
[46] Calculated 1550 nm	45 μ m / 750 nm	-0.58 dB	$\pm 1.0 \mu$ m	$\pm 1.0 \mu$ m	UHNA-3 (4.1 \pm 0.3 μ m)	300 \times 1000 nm / shadow mask
[46] Measured 1550 nm		-1.47 dB	-	-		
[47] Calculated 1550 nm	76 μ m / 200 nm	-0.29 dB	$\pm 2.0 \mu$ m	$\pm 2.0 \mu$ m	UHNA-3 (4.1 \pm 0.3 μ m)	500 \times 2000 nm / a single step litho
[47] Measured 1550 nm		-0.36 dB	$\pm 3.5 \mu$ m	$\pm 3.3 \mu$ m		
Current work Calculated 1550 nm	360 μ m / 275 nm	-2.52 dB	$\pm 3.2 \mu$ m	$\pm 2.9 \mu$ m	SMF-28 (10.5 \pm 0.5 μ m)	220 \times 1200 nm / double step litho, 5 μ m oxide thickness
	360 μ m / 275 nm	-1.55 dB	$\pm 2.0 \mu$ m	$\pm 1.5 \mu$ m	SM1500es (4.0 \pm 0.5 μ m)	
	360 μ m / 275 nm	-0.75 dB	$\pm 1.7 \mu$ m	$\pm 1.3 \mu$ m	UHNA-7 (3.2 \pm 0.3 μ m)	
	360 μ m / 275 nm	-0.55 dB	$\pm 1.5 \mu$ m	$\pm 1.2 \mu$ m	LPMFs (2.5 \pm 0.3 μ m)	
Current work Measured 1550 nm	360 μ m / 275 nm	-3.28 dB	$\pm 2.8 \mu$ m	$\pm 2.4 \mu$ m	SMF-28 (10.5 \pm 0.5 μ m)	
	360 μ m / 275 nm	-0.97 dB	$\pm 1.4 \mu$ m	$\pm 1.1 \mu$ m	SM1500es (4 \pm 0.5 μ m)	
	360 μ m / 275 nm	-0.81 dB	$\pm 1.2 \mu$ m	$\pm 0.8 \mu$ m	UHNA-7 (3.2 \pm 0.3 μ m)	
	360 μ m / 275 nm	-1.25 dB	$\pm 0.9 \mu$ m	$\pm 0.7 \mu$ m	LPMFs (2.5 \pm 0.3 μ m)	
Current work Calculated Multi-tip taper 1550 nm	265 μ m / 8.55 μ m	-0.51 dB	$\pm 5 \mu$ m	$\pm 3 \mu$ m	SMF-28 (10.5 \pm 0.5 μ m)	220 \times 1200 nm / double step litho, 8 μ m oxide thickness
Current work Measured Multi-tip taper 1550 nm		-1.50 dB	-	-		
Current work Calculated 1550 nm	280 μ m / 500 nm	-0.10 dB	$\pm 1.2 \mu$ m	$\pm 0.9 \mu$ m	UHNA-7 (3.2 \pm 0.3 μ m)	
Current work Measured 1550 nm		-0.15 dB	-	-		

Currently, the best achieved efficiency of -0.17 dB was demonstrated by the adiabatic Si₃N₄ coupler based on a taper with a length of 500 μ m for UHNA-3 fiber/100 \times 900 nm

waveguide interface, cleaved with a good cleaving position tolerance [37].

This paper serves as a tutorial on finding the best repeatable wafer-scale compatible coupling strategy for the Si₃N₄

platform. The entire Si_3N_4 waveguide fabrication comprises waveguide fabrication and plasma dicing based on deep silicon etching, which provides optical quality chip edge forming. In this article a universal approach for taper design is for standard fiber/chip coupling are calculated to be ~ 0.51 dB and measured to be ~ 1.50 dB for 1550 nm per connection.

COUPLING STRATEGIES

Tapered waveguide simulation. For PICs, low-loss edge coupling special waveguide structures, which serve as mode size converters, are used [48,49]. The optical mode size and shape change during propagation through the tapered waveguide to achieve higher coupling efficiency between two modes with different cross-sections. They are designed to operate adiabatically: the waveguide local first-order mode should propagate through the tapered waveguide while undergoing relatively little mode conversion compared with the higher-order modes or radiation modes. This adiabatic operation is realized in the taper design by gradually increasing the taper cross-section size and decreasing the mode size from typical diameter of 5-10 μm in fiber to the order of several microns in the waveguide. Different designs of adiabatic tapers have been proposed for Si_3N_4 platforms, including linear [48], exponential [22], parabolic [50], and multi-sectional tapers [24,25]. Most often, a linear waveguide tapers were used. In this linear adiabatic taper mode, conversion occurs more easily in the wider portion [22].

For low-loss transmission, the linear taper can be extended to be long enough to ensure adiabatic propagation. However, a longer taper could lead to higher propagation losses. This problem becomes more critical when the two modes connected by the linear taper possess higher cross-sectional differences. In this case, the taper starts with a width that is much narrower than one of the waveguide. This makes the taper wall roughness' influence on losses much more noticeable. Thus, the taper length should be reduced to ensure the lowest possible losses and to reduce the device footprint. Modeling started with the waveguide geometry determination to ensure on fundamental mode excitation (Figure 2a). Modeling was carried out in Ansys Lumerical FDE, on the basis of which a waveguide width of 1200 nm was chosen. To determine the optimal taper geometry, modeling was performed in Ansys Lumerical FDTD based on the numerical solution of Maxwell's equations. The taper 3D model is shown in Figure 1a.

The length of the fabricated tapers varied from 200 μm to 520 μm , (Figure 2 (c-f)). In turn, the width at the beginning of the taper varied from 50 to 500 nm with a waveguide width of 1200 nm. The smallest feature size is determined by the technological capabilities of electron lithography technology. The graph shows the dependance obtained during the simulation for the different optical fibers. In this study, the taper length was 360 μm for high transmission maintaining a relatively small device footprint. To standardize the technological process, a taper geometry (width 280 nm, length 360 μm) was chosen to ensure maximum coupling efficiency for all types of optical fibers. The light was emitted from the fiber onto the mode size converter, as shown in the top-down view in Figure 2h.

presented, which was used to simulate several types of inverted taper couplers. The coupling losses per coupler for the UHNA-7 fiber/chip coupling are calculated to be ~ 0.75 dB and measured to be ~ 0.81 dB for 1550 nm per connection.

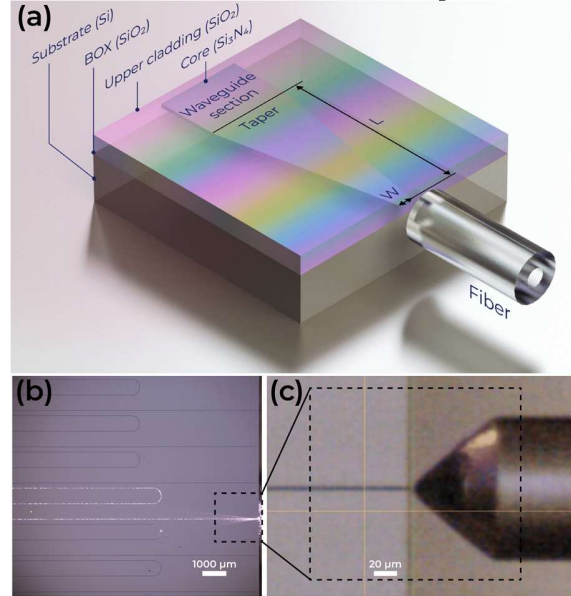


Figure 1. 3D visualization of coupled taper with fiber (a), Light propagation through the waveguide (b), Coupling of lensed fiber with chip facet (c).

Edge facet. To provide high taper coupling efficiency, the PIC dies are typically polished to obtain high optical grade quality edges [51]. Although this process works well with small chip sizes, it's scaling up to wafer level is impractical. There is also used the process of silicon dioxide thick layers wet etching, but it is anisotropic, that negatively affects the quality of the optical facets [52]. Other solutions for PICs optical facets fabrication need to be investigated. A promising technology is the reactive plasma dicing [53].

We previously demonstrated the lowest propagation losses currently available in the near-infrared wavelength (as low as 0.55 dB/cm) in single-mode Si_3N_4 submicron waveguides (220x550 nm) [54]. Our study continues the previous research and presents a plasma-based process for optical grade edge facets fabrication. The fabrication process of low-loss silicon nitride photonic integrated circuits with light coupling through edge couplers is shown in Figure 3. The presented technology is used to dice a chip, that consists of 220-nm-thick stoichiometric low-pressure chemical vapor Si_3N_4 layer grown on the 525- μm silicon substrate oxidized with the 2.5- μm thickness and covered with 2.5- μm oxide. A standard sequence of basic operations is involved for fabrication (Figure 3). First, the waveguide structure alignment markers were patterned using electron-beam lithography. The pattern is then transferred to the Si_3N_4 device layer by reactive ion plasma etching (RIE) [55]. After nanotopology fabrication, the chip is plasma diced. The dicing process consists of the following stages: surface preparation, photoresist spin coating, photolithography, photoresist development, SiO_2 - Si_3N_4 - SiO_2 thin film stack etching, photoresist removal, and silicon etching by the Bosch process [55].

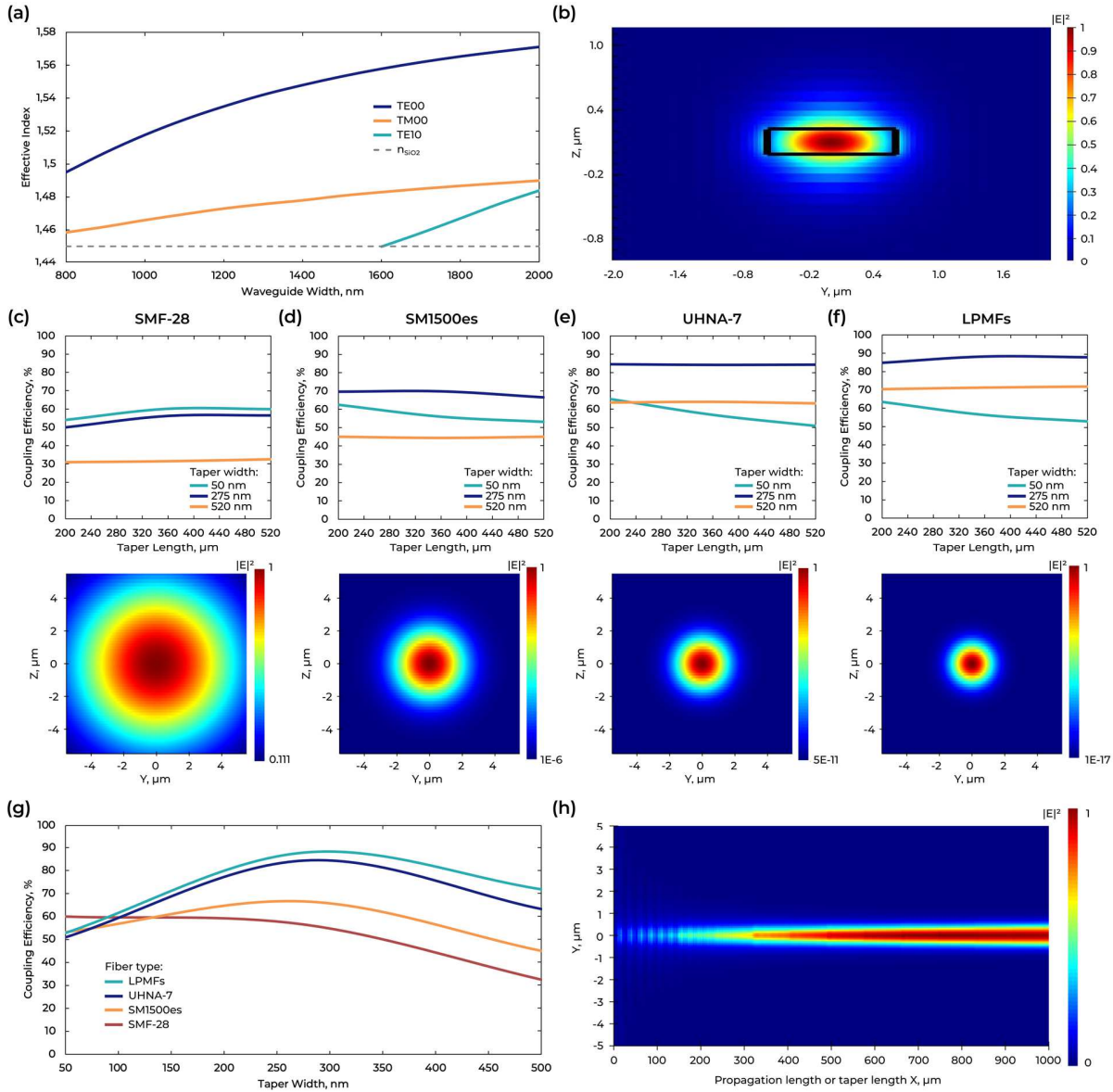


Figure 2. Calculation of Si₃N₄ effective index of modes excited in a waveguide as a function of waveguide width (a), Fundamental mode excited in the waveguide with 220x1200 nm cross section (b), Calculation of the taper length at different width for different fiber types with wavelength 1550 nm (c-f), Calculation of the taper width with fixed length of taper (360 μm) for different fiber types with wavelength 1550 nm (g) and simulation of mode propagation for lensed fiber (h).

To pattern the silicon dioxide layer, 5 μm thick SPR220 photoresist was used. Patterning processes were performed using laser lithography. The topology was then transferred to the multilayer stack (SiO₂-Si₃N₄-SiO₂) with reactive ion etching. The next step was silicon wafer dicing using the Bosch process. Optical microscopy and scanning electron microscopy were used to characterize the samples and control process quality.

The mentioned above SPR220 positive photoresist pattern transfer mask with an anti-reflective layer using laser lithography should have a vertical profile to be further used for

vertical edge etching. It lets avoiding the effect of refraction during light coupling from the optical fibers to the chip. Resist thickness was chosen based on plasma etching process selectivity to ensure etching of SiO₂-Si₃N₄-SiO₂ layers with a total thickness of 5.2 μm. The laser lithography dose and focus were varied to obtain the pattern mask vertical profile. For the structural vertical angle exposure in thick resist layers, multi-pass lithography was used. In this study, four- and six- pass algorithms were applied (Figure 4b).

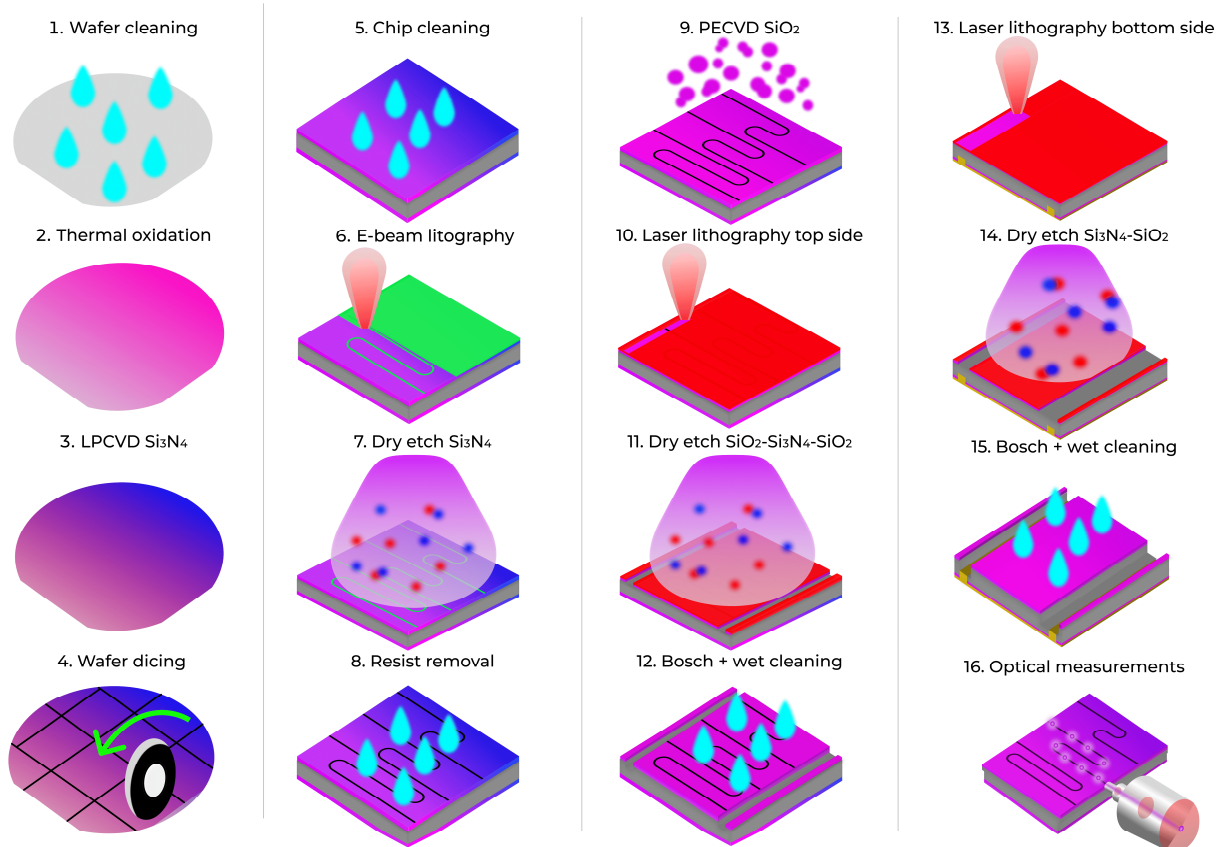


Figure 3. Si_3N_4 PICs with edge coupling fabrication process.

The clear maximum can be seen in Figure 5b. The 88.7° resist sidewall angle corresponds to the following lithography regime: 60 mW laser power, 4 passes, -15 % focus. The found regime was further used in etching technology development.

Etching was performed using the ICP-RIE system. For etching thick layers of silicon dioxide (more than $5\ \mu\text{m}$) with a vertical profile ($90\pm 0.5^\circ$) and a smooth edge surface, the CHF_3 process gas was selected. During etching process, the CF_x polymer film is deposited on the side walls during the etch process and protects the side surface, simultaneously providing a vertical profile [56,57]. In addition, Ar was added to the plasma to stimulate the etching process.

An increase in the plasma source power in the CHF_3/Ar plasma mixture from 1000 W to 2500 W led to an increase in selectivity from 0.9 to 1.3 due to a decrease in the bias voltage. At the same time, the profile angle increased in the positive direction from 88.7° to 92.5° because of the growth

of radicals and, as a result, of the process chemical components [58].

An increase in stage power in the range from 50 to 90 W leads to an increase in the bias voltage and an increase in the ionic etching component, which results in a general decrease in selectivity with the local minimum observed at 70 W. With an increase in the process ionic component, the profile angle narrows toward anisotropy (from 88.5° to 86.5°), which, along with the ICP source, is a fairly effective tool for controlling both selectivity and profile angle.

A decrease in the working pressure reduces the total number of collisions within the plasma mixture, thereby increasing the overall direction of the mixture toward the substrate. Through such effects, the profile angle became more negative, and the overall selectivity was reduced because of the presence of more energetic ions in the mixture composition [58].

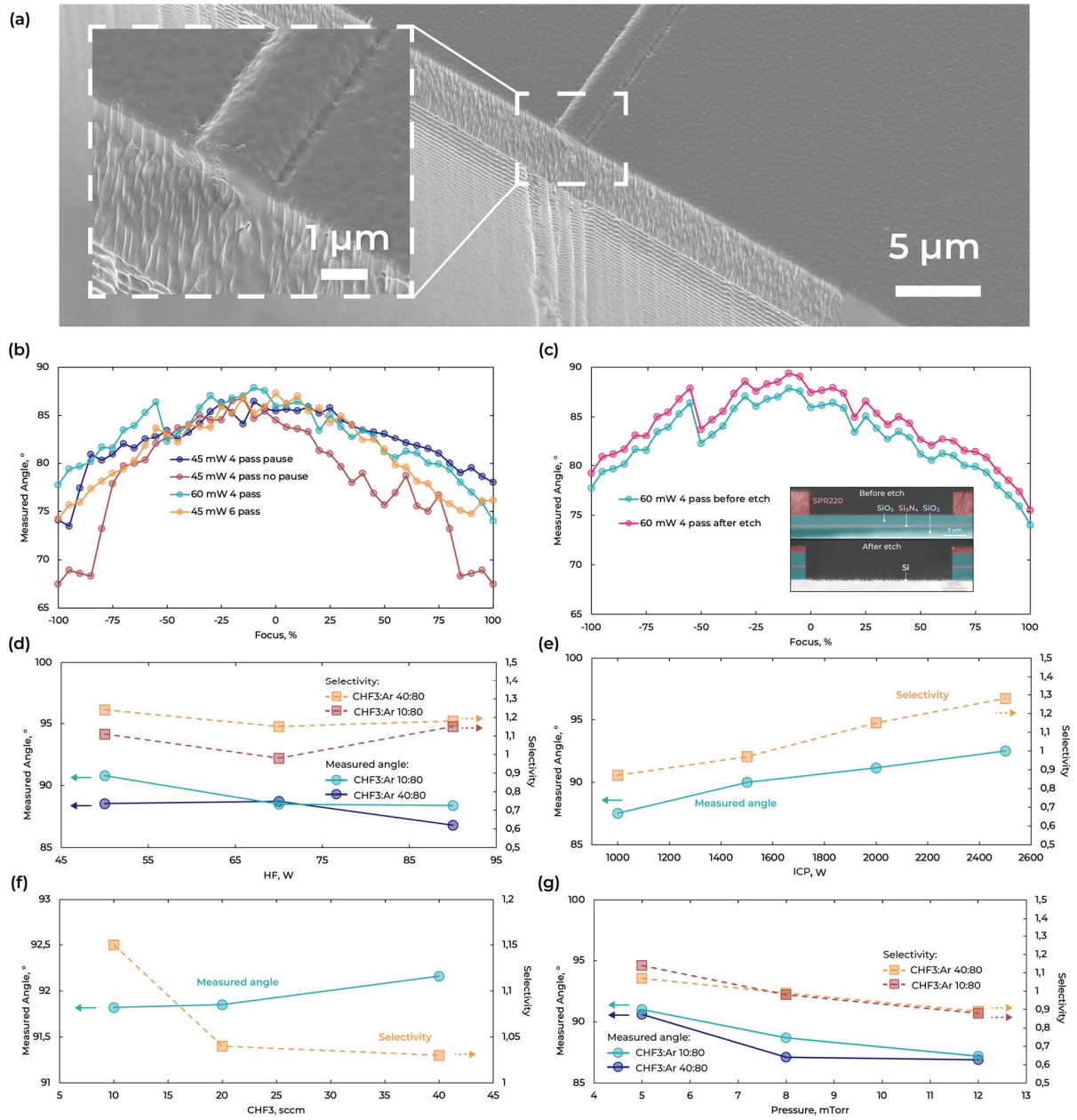


Figure 4. SEM image of the fabricated edge coupler (a), dependence of the resist sidewall angle on the laser lithography power and focus value (b), sidewall angle comparison before and after etching (c), $\text{SiO}_2\text{-Si}_3\text{N}_4\text{-SiO}_2$ layers sidewall angle and selectivity dependence on gas mixture (d), $\text{SiO}_2\text{-Si}_3\text{N}_4\text{-SiO}_2$ layers sidewall angle and selectivity dependence on ICP power (e), $\text{SiO}_2\text{-Si}_3\text{N}_4\text{-SiO}_2$ layers sidewall angle and selectivity dependence on CHF_3 amount (f) and $\text{SiO}_2\text{-Si}_3\text{N}_4\text{-SiO}_2$ layers sidewall angle and selectivity dependence on chamber pressure (g).

Increasing the amount of the main etching gas CHF_3 in the mixture (from 10 sccm to 40 sccm) did not significantly affect the overall process dynamics in terms of the profile angle and remains in the range from 91.85° to 92.15° , which could be considered insignificant. However, a significant increase in the etch rate (from 150 nm/min to 230 nm/min) and a slight decrease in selectivity (from 1.15 to 1.03) were observed. Profile angle preservation with an increase in the

etching rate could be associated with preservation of the passivation/etching balance on the channel side walls and simultaneous increase in the ionic and fluorine radicals [59].

Based on the obtained equations, the following etching regime was chosen: stage power 50 W, ICP power 2000 W, pressure 5 mTorr, CHF_3 flow 40 sccm, and Ar flow 80 sccm.

Coupling efficiency improvement. Thicker bottom and cladding SiO₂ layer help to release the vertical mode mismatch and reflection from Si layer. The comparison diagram of value SiO₂ thickness and taper type on coupling efficiency is shown on Figure 5.

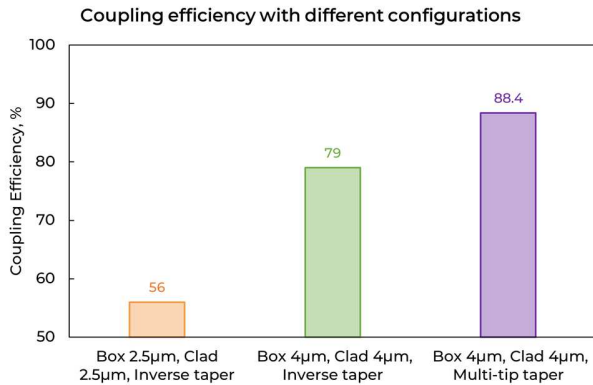


Figure 5. Coupling efficiency with different configurations.

To fabricate a photonic integrated circuit with thick oxide layers by deep etching, it is necessary to use a thicker resist layer. The process of forming a resist with a thickness of 9.5 µm and a non-uniformity of 2% was found. For a resist with a thickness of 9.5 µm, a similar work was carried out on selecting the exposure dose and focus as in the previous section. The 89.0° resist sidewall angle corresponds to the following lithography regime: 60 mW laser power, 8 passes, -25 % focus. The figure shows the resist profile angle after the laser lithography step and the profile angle of the optical layers after the etching steps.

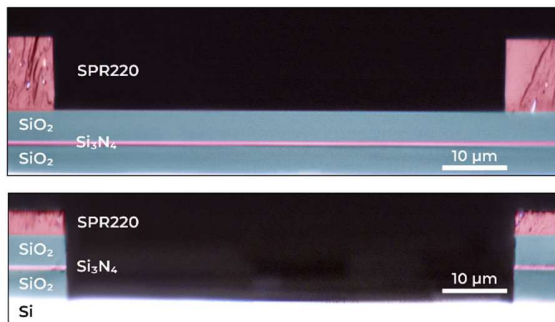


Figure 6. Angle profile after laser lithography and after dry etch.

Another approach to reduce coupling losses is to use a multi-tip taper. Improving the geometry of the edge couplers by increasing the tip number often makes improvements to the coupling performance between optical fiber and optical channel on chip [60]. It is known that the mode field diameter of SMF28 fiber is 10 µm, so a wide taper will allow capturing more optical power from the fiber. In addition, the trident-shaped multi-taper will reduce the mismatch of the effective indices of the fiber and the multi-taper.

The proposed multi-taper design is shown in Figure 7. The design consists of three sections (Figure 7): a trident, a transition region, and an adiabatic taper. The tip length, tip start width, connection length and taper length with highest coupling efficiency are calculated by Ansys Lumerical FDTD. The results are shown in Figure 7. The chosen geometry of

multi-taper has the following parameters: tip length = 220 µm, tip initial width = 100 nm, connection length = 5 µm and taper length = 40 µm. The calculated and measured coupling losses with such multi-taper were 0.51 dB and 1.5 dB, respectively.

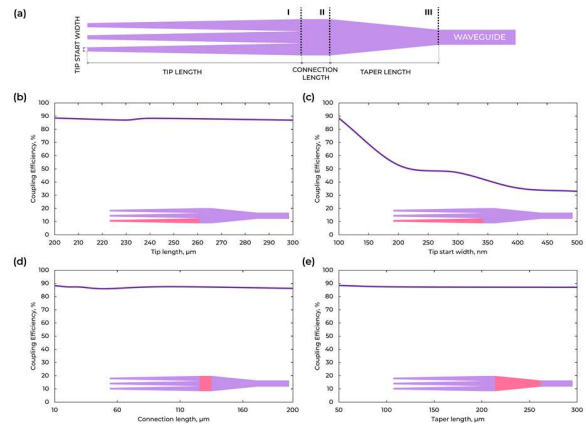


Figure 7. Visualization of multi-tip taper with separation on parts (a). Calculation of the tip length for multi-tip taper (b). Calculation of the tip start width for multi-tip taper (c). Calculation of the connection length for multi-tip taper (d). Calculation of the taper length for multi-tip taper (e).

CHARACTERIZATION

Cut-back measurement. To measure the I/O efficiency, an automated assembly system equipped with a 5-nm resolution 12-axis alignment drive, 935 nm and 1550 nm wavelength laser sources, and an optical power meter was used. This system made it possible to measure internal optical losses and coupling efficiency using the output power values of structures of various lengths.

The cut-back propagation loss analysis [61, 62] in the fabricated Si₃N₄ waveguides was performed for an integrated circuit. The light was coupled out from the polished FAU through PIC to the power detector. Propagation losses were measured on the test photonic integrated circuits with varying length structures for loss measurement and are shown in Figure 8a.

Figure 8b presents the measured coupling losses for different fiber type and different thickness SiO₂ layers. The lowest coupling losses for inverted taper of about -0.81 dB were observed for UHNA-7 fiber. For higher cladding oxide thickness we observed losses minimization due to -0.15 dB for UHNA-7 fiber.

OFDR measurements. Reflectometry is widely used in fiber optics to probe the local reflectivity of waveguides and devices with respect to propagation distance [63]. With a point-to-point resolution of about 10 µm and detection sensitivity of -130 dB over 30 m of propagation, coherent optical backscattering reflectometry (OFDR) is a particularly useful technique in characterizing waveguides and devices at the planar scale [64,65]. In the OFDR, a continuous wave laser source is scanned over several terahertz in frequency or, equivalently, several tens of nanometers in wavelength. A larger scan range improves the measurement spatial resolution according to the following expression:

$$D_{min} \cong \frac{c}{2n_g|f_{start} - f_{end}|} = \frac{\lambda_{start}\lambda_{end}}{2n_g|\lambda_{start} - \lambda_{end}|}$$

where D_{\min} is the minimum distance between the two data points, c is the speed of light, ng is the group index, f_{start} and λ_{start} are the source frequency and wavelength at the scanning start, respectively, and f_{end} and λ_{end} are the source frequency and wavelength at the scanning end [32]. However, all parameters derived from the spatial domain data are then averaged over the measurement scan spectral range. If the parameter spectral dependence is set, the rectangular window function can be applied to data in the spectral domain to narrow the included spectral range. This window could be moved across the measurement's full spectral range, making it possible to extract the parameter at each window position and obtain the parameter spectral dependence from a single OFDR scan. Because narrowing data in the frequency domain decreases the measurement spatial resolution according to Eq. (2), a tradeoff appears between the spectral averaging, which could distort the actual spectral dependence

and the measurement accuracy. In this study, a FDTD window width of 10 nm is used to extract the spectrally dependent measurements of the coupling loss propagation loss.

Figure 8d shows the OFDR data from two UHNA-7 fibers coupled to waveguides (10 cm long). The data was not filtered in the spectral domain, and a moving average filter with 100-datapoint or ~ 1 mm window size was applied in the spatial domain to reduce the backscatter amplitude deviation. Before OFDR scanning, fiber-to-chip coupling was maximized using an OFDR source laser and an optical power meter. The dashed lines in Figure 8d indicate the mean backscatter levels in waveguide. The difference between these two levels of 5.96 dB includes the total return loss between the two fibers, or:

$$RL_{dB}^{\text{total}} = 2IL_{dB}^{\text{total}} = 2(IL_{dB}^{\text{fiber-to-chip}} + IL_{dB}^{\text{propagation}} + IL_{dB}^{\text{fiber-to-chip}})$$

where RL_{dB}^{total} is the total return loss in dB, total IL_{dB} is the total insertion loss, fiber-to-chip IL_{dB} is the fiber-to-chip insertion loss per facet, and propagation IL_{dB} is the total propagation insertion loss.

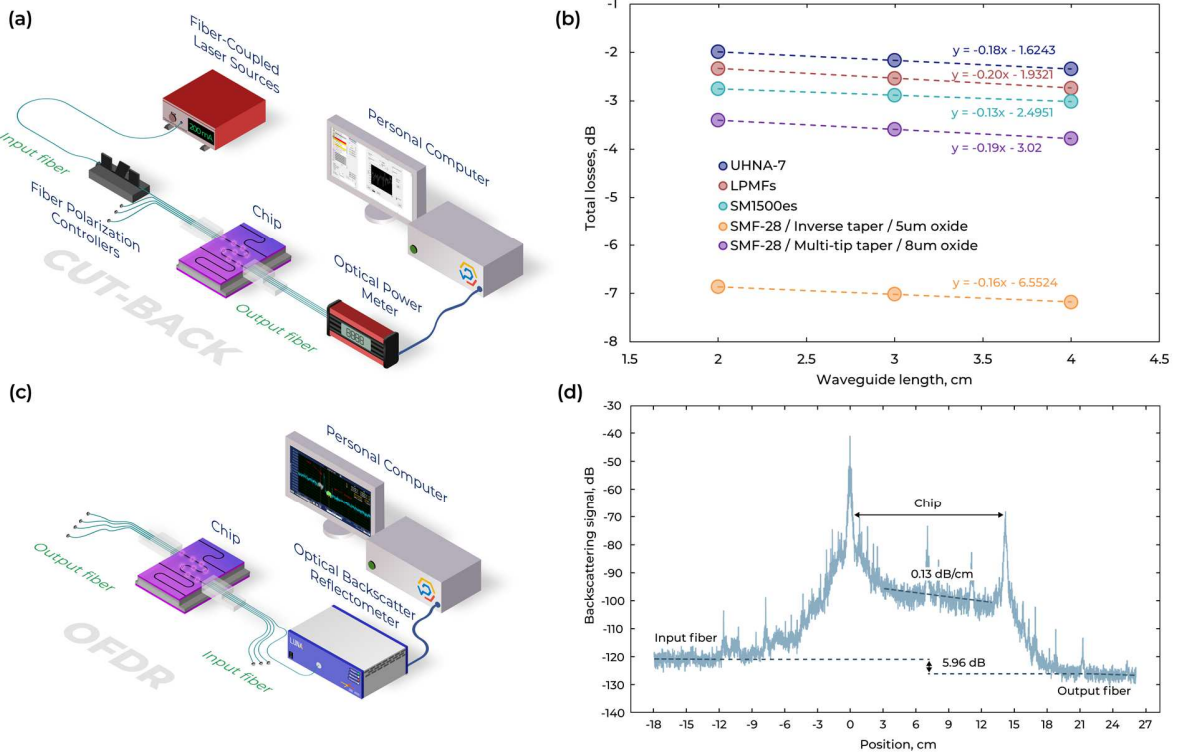


Figure 8. Schematic of the measurement setup for cut-back characterization (a); Propagation losses measured by the cut-back calculated: $y = k \times x + b$; $k = \text{propagation losses}$, $b = \text{coupling losses}$ for wavelength 1550 nm (b); Schematic of the measurement setup for OFDR characterization (c) and OFDR characterization along the waveguide. The dashed line shows the linear fit of the waveguide reflections (d).

The measured data is linearly fitted to find propagation losses (Figure 8d). Based on OFDR characterization, the propagation insertion loss is 0.13 dB/cm and fiber-to-chip insertion loss per facet is 0.84 dB.

CONCLUSION

This study presents a universal strategy for repeatable wafer-scale PIC low-loss edge coupling. For a coupling platform, we present a tutorial on the design, manufacturing, and char-

acterization of lithographically defined optical coupling facets using an ICP dry etching technique. Fabrication process optimization allowed us to obtain the 89 degrees optical grade facet that provides coupling losses lower than 1 dB for a set of optical fibers that agrees well with the simulation results. To reduce propagation insertion losses, fabrication process should include chemical-mechanical polishing and long-term annealing steps. We believe that this research would be useful for a wide PIC community.

AUTHOR INFORMATION

Corresponding Author

Ilya A. Rodionov - Shukhov Labs, Quantum Park, Bauman Moscow State Technical University, Moscow 105005, Russia; Dukhov Automatics Research Institute, Moscow 127055, Russia; orcid.org/0000-0002-8931-5142; Email: irodionov@bmstu.ru

Authors

Sergey A. Avdeev – Shukhov Labs, Quantum Park, Bauman Moscow State Technical University, Moscow 105005, Russia; Dukhov Automatics Research Institute, Moscow 127055, Russia; orcid.org/0000-0002-7296-367X; Email: avdeevss@bmstu.ru

Aleksandr S. Baburin - Shukhov Labs, Quantum Park, Bauman Moscow State Technical University, Moscow 105005, Russia; Dukhov Automatics Research Institute, Moscow 127055, Russia; orcid.org/0000-0003-2806-018X; Email: baburin@bmstu.ru

Evgeniy V. Sergeev - Shukhov Labs, Quantum Park, Bauman Moscow State Technical University, Moscow 105005, Russia; orcid.org/0000-0002-2272-2624; Email: sergeev_e@bmstu.ru

Alexei B. Kramarenko - Shukhov Labs, Quantum Park, Bauman Moscow State Technical University, Moscow 105005, Russia; orcid.org/0009-0003-2217-8459; Email: kramarenko@bmstu.ru

Arseniy V. Belyaev - Shukhov Labs, Quantum Park, Bauman Moscow State Technical University, Moscow 105005, Russia; Email: arsbel99@gmail.com

Danil V. Kushnev - Shukhov Labs, Quantum Park, Bauman Moscow State Technical University, Moscow 105005, Russia; Email: dvkushnev@gmail.ru

Kirill A. Buzaverov - Shukhov Labs, Quantum Park, Bauman Moscow State Technical University, Moscow 105005, Russia; orcid.org/0000-0002-5550-6880; Email: kirillbuz@bmstu.ru

Ilya A. Stepanov - Shukhov Labs, Quantum Park, Bauman Moscow State Technical University, Moscow 105005, Russia; orcid.org/0000-0002-6533-4373; Email: stepanovia@bmstu.ru

Vladimir V. Echeistov - Shukhov Labs, Quantum Park, Bauman Moscow State Technical University, Moscow 105005, Russia; orcid.org/0000-0002-2258-9843; Email: Wecheistov@bmstu.ru

Sergey V. Bukatin - Shukhov Labs, Quantum Park, Bauman Moscow State Technical University, Moscow 105005, Russia; orcid.org/0009-0006-0557-2659; Email: bukatin@bmstu.ru

Ali Sh. Amiraslanov - Shukhov Labs, Quantum Park, Bauman Moscow State Technical University, Moscow 105005,

Russia; orcid.org/0009-0003-1744-6420; Email: amiraslanovash@student.bmstu.ru

Evgeniy S. Lotkov - Shukhov Labs, Quantum Park, Bauman Moscow State Technical University, Moscow 105005, Russia; orcid.org/0000-0001-5386-7837; Email: lotevg@bmstu.ru

Dmitry A. Baklykov - Shukhov Labs, Quantum Park, Bauman Moscow State Technical University, Moscow 105005, Russia; orcid.org/0000-0002-3595-7510; Email: dima_baklykov@bmstu.ru

Author Contributions

Ilya A. Rodionov initiated and directed the work. Sergey S. Avdeev conducted the design, fabrication, measurement and analyzed the experimental data. Aleksandr S. Baburin supervised the project. The manuscript was discussed and corrected by all authors.

Notes

The authors declare no competing financial interest.

ACKNOWLEDGMENT

Technology was developed and samples were fabricated at Quantum Park (BMSTU Nanofabrication Facility, Shukhov Labs, FMNS REC, ID 74300).

REFERENCES

- (1) Malhouitre, S.; Fowler, D.; Garcia, S.; Lemonnier, O.; Tyler, N.; Rabaud, W. Silicon Nitride Photonic Platform for LIDAR Applications. In *2018 IEEE 15th International Conference on Group IV Photonics (GFP)*; **2018**; pp 1–2. <https://doi.org/10.1109/GROUP4.2018.8478704>.
- (2) Rodionov, I. A.; Baburin, A. S.; Zverev, A. V.; Philippov, I. A.; Gabidulin, A. R.; Dobronosova, A. A.; Ryzhova, E. V.; Vinogradov, A. P.; Ivanov, A. I.; Maklakov, S. S.; Baryshev, A. V.; Trofimov, I. V.; Merzlikin, A. M.; Orlikovsky, N. A.; Rizhikov, I. A. Mass Production Compatible Fabrication Techniques of Single-Crystalline Silver Metamaterials and Plasmonics Devices. In *Metamaterials, Metadevices, and Metasystems* **2017**; Engheta, N., Noginov, M. A., Zheludev, N. I., Eds.; SPIE, 2017; Vol. 10343, p 1034337. <https://doi.org/10.1117/12.2271643>.
- (3) Baburin, A. S.; Ivanov, A.; Trofimov, I.; Dobronosova, A.; Melentiev, P.; Balykin, V.; Moskalev, D.; Pishchimova, A.; Ganieva, L.; Ryzhikov, I.; Rodionov, I. Highly Directional Plasmonic Nanolaser Based on High-Performance Noble Metal Film Photonic Crystal; SPIE-Intl Soc Optical Eng, 2018; p 159. <https://doi.org/10.1117/12.2307572>.
- (4) Yankovskii, G. M.; Komarov, A. V.; Puz'ko, R. S.; Baryshev, A. V.; Afanas'ev, K. N.; Boginskaya, I.

- A.; Bykov, I. V.; Merzlikin, A. M.; Rodionov, I. A.; Ryzhikov, I. A. Structural and Optical Properties of Single and Bilayer Silver and Gold Films. *Physics of the Solid State* **2016**, *58* (12), 2503–2510. <https://doi.org/10.1134/S1063783416120349>.
- (5) Baburin, A. S.; Ivanov, A. I.; Ryzhikov, I. A.; Trofimov, I. V.; Gabidullin, A. R.; Moskalev, D. O.; Panfilov, Y. V.; Rodionov, I. A. Crystalline Structure Dependence on Optical Properties of Silver Thin Film over Time. In *2017 Progress In Electromagnetics Research Symposium - Spring (PIERS)*; 2017; pp 1497–1502. <https://doi.org/10.1109/PIERS.2017.8261984>.
- (6) Baburin, A. S.; Moskalev, D. O.; Lotkov, E. S.; Sorokina, O. S.; Baklykov, D. A.; Avdeev, S. S.; Buzaverov, K. A.; Yankovskii, G. M.; Baryshev, A. V.; Ryzhikov, I. A.; Rodionov, I. A. Evolutionary Selection Growth of Silver Films for Low-Loss Nanophotonic Devices. *Surfaces and Interfaces* **2023**, *39*, 102897. <https://doi.org/10.1016/j.surfin.2023.102897>.
- (7) Lagarkov, A.; Boginskaya, I.; Bykov, I.; Budashov, I.; Ivanov, A.; Kurochkin, I.; Ryzhikov, I.; Rodionov, I.; Sedova, M.; Zverev, A.; Sarychev, A. K. Light Localization and SERS in Tip-Shaped Silicon Metasurface. *Opt. Express* **2017**, *25* (15), 17021–17038. <https://doi.org/10.1364/OE.25.017021>.
- (8) Hoi, H.; Rezaie, S. S.; Gong, L.; Sen, P.; Zeng, H.; Montemagno, C.; Gupta, M. Biofunctionalized Silicon Nitride Platform for Sensing Applications. *Biosens Bioelectron* **2018**, *102*, 497–503. <https://doi.org/https://doi.org/10.1016/j.bios.2017.11.059>.
- (9) Lotkov, E. S.; Baburin, A. S.; Ryzhikov, I. A.; Sorokina, O. S.; Ivanov, A. I.; Zverev, A. V.; Ryzhkov, V. V.; Bykov, I. V.; Baryshev, A. V.; Panfilov, Y. V.; Rodionov, I. A. ITO Film Stack Engineering for Low-Loss Silicon Optical Modulators. *Sci Rep* **2022**, *12* (1). <https://doi.org/10.1038/s41598-022-09973-5>.
- (10) Stepanov, I. A.; Baburin, A. S.; Kushnev, D. V.; Sergeev, E. V.; Shmonina, O. I.; Matanin, A. R.; Echeistov, V. V.; Ryzhikov, I. A.; Panfilov, Y. V.; Rodionov, I. A. Sputtered NbN Films for Ultrahigh Performance Superconducting Nanowire Single-Photon Detectors. *APL Mater* **2024**, *12* (2). <https://doi.org/10.1063/5.0188420>.
- (11) Taballione, C.; Wolterink, T. A. W.; Lugani, J.; Eckstein, A.; Bell, B. A.; Grootjans, R.; Visscher, I.; Geskus, D.; Roeloffzen, C. G. H.; Renema, J. J.; Walmsley, I. A.; Pinkse, P. W. H.; Boller, K.-J. 8×8 Reconfigurable Quantum Photonic Processor Based on Silicon Nitride Waveguides. *Opt Express* **2019**, *27* (19), 26842. <https://doi.org/10.1364/oe.27.026842>.
- (12) Weng, H.-C.; Monroy-Ruz, J.; Matthews, J. C. F.; Rarity, J. G.; Balram, K. C.; Smith, J. A. Heterogeneous Integration of Solid-State Quantum Systems with a Foundry Photonics Platform. *ACS Photonics* **2023**, *10* (9), 3302–3309. <https://doi.org/10.1021/acsphotonics.3c00713>.
- (13) Xiang, C.; Jin, W.; Bowers, J. E. Silicon Nitride Passive and Active Photonic Integrated Circuits: Trends and Prospects. *Photonics Res* **2022**, *10* (6), A82. <https://doi.org/10.1364/PRJ.452936>.
- (14) Guo, X.; Ji, X.; Yao, B.; Tan, T.; Chu, A.; Westreich, O.; Dutt, A.; Wong, C.; Su, Y. Ultra-Wideband Integrated Photonic Devices on Silicon Platform: From Visible to Mid-IR. *Nanophotonics* **2023**, *12* (2), 167–196. <https://doi.org/10.1515/nanoph-2022-0575>.
- (15) Baets, R.; Subramanian, A. Z.; Clemmen, S.; Kuyken, B.; Bienstman, P.; Thomas, N. Le; Roelkens, G.; Thourhout, D. Van; Helin, P.; Severi, S. Silicon Photonics: Silicon Nitride versus Silicon-on-Insulator. In *Optical Fiber Communication Conference*; OSA, 2016; p Th3J.1. <https://doi.org/10.1364/OFC.2016.Th3J.1>.
- (16) Muñoz, P.; Micó, G.; Bru, L.; Pastor, D.; Pérez, D.; Doménech, J.; Fernández, J.; Baños, R.; Gargallo, B.; Alemany, R.; Sánchez, A.; Cirera, J.; Mas, R.; Domínguez, C. Silicon Nitride Photonic Integration Platforms for Visible, Near-Infrared and Mid-Infrared Applications. *Sensors* **2017**, *17* (9), 2088. <https://doi.org/10.3390/s17092088>.
- (17) Bakir, B. Ben; de Gyves, A. V.; Orobtochouk, R.; Lyan, P.; Porzier, C.; Roman, A.; Fedeli, J.-M. Low-Loss (<1 DB) and Polarization-Insensitive Edge Fiber Couplers Fabricated on 200-Mm Silicon-on-Insulator Wafers. *IEEE Photonics Technology Letters* **2010**, *22* (11), 739–741. <https://doi.org/10.1109/LPT.2010.2044992>.
- (18) Hatori, N.; Shimizu, T.; Okano, M.; Ishizaka, M.; Yamamoto, T.; Urino, Y.; Mori, M.; Nakamura, T.; Arakawa, Y. A Hybrid Integrated Light Source on a Silicon Platform Using a Trident Spot-Size Converter. *Journal of Lightwave Technology* **2014**, *32* (7), 1329–1336. <https://doi.org/10.1109/JLT.2014.2304305>.
- (19) Urino, Y.; Usuki, T.; Fujikata, J.; Ishizaka, M.; Yamada, K.; Horikawa, T.; Nakamura, T.; Arakawa, Y. High-Density and Wide-Bandwidth Optical Interconnects with Silicon Optical Interposers [Invited]. *Photonics Res* **2014**, *2* (3), A1. <https://doi.org/10.1364/PRJ.2.0000A1>.

- (20) Cheben, P.; Schmid, J. H.; Wang, S.; Xu, D.-X.; Vachon, M.; Janz, S.; Lapointe, J.; Painchaud, Y.; Picard, M.-J. Broadband Polarization Independent Nanophotonic Coupler for Silicon Waveguides with Ultra-High Efficiency. *Opt Express* **2015**, *23* (17), 22553. <https://doi.org/10.1364/OE.23.022553>.
- (21) Papes, M.; Cheben, P.; Benedikovic, D.; Schmid, J. H.; Pond, J.; Halir, R.; Ortega-Moñux, A.; Wangüemert-Pérez, G.; Ye, W. N.; Xu, D.-X.; Janz, S.; Dado, M.; Vašínek, V. Fiber-Chip Edge Coupler with Large Mode Size for Silicon Photonic Wire Waveguides. *Opt Express* **2016**, *24* (5), 5026. <https://doi.org/10.1364/OE.24.005026>.
- (22) Atsumi, Y.; Yoshida, T.; Omoda, E.; Sakakibara, Y. Broad-Band Surface Optical Coupler Based on a SiO₂-Capped Vertically Curved Silicon Waveguide. *Opt Express* **2018**, *26* (8), 10400. <https://doi.org/10.1364/OE.26.010400>.
- (23) Shoji, T.; Tsuchizawa, T.; Watanabe, T.; Yamada, K.; Morita, H. Low Loss Mode Size Converter from 0.3 μm Square Si Wire Waveguides to Singlemode Fibres. *Electron Lett* **2002**, *38* (25), 1669. <https://doi.org/10.1049/el:20021185>.
- (24) Almeida, V. R.; Panepucci, R. R.; Lipson, M. Nanotaper for Compact Mode Conversion. *Opt Lett* **2003**, *28* (15), 1302. <https://doi.org/10.1364/OL.28.001302>.
- (25) Roelkens, G.; Dumon, P.; Bogaerts, W.; Thourhout, D. Van; Baets, R. Efficient Silicon-on-Insulator Fiber Coupler Fabricated Using 248-Nm-Deep UV Lithography. *IEEE Photonics Technology Letters* **2005**, *17* (12), 2613–2615. <https://doi.org/10.1109/LPT.2005.859132>.
- (26) McNab, S.; Moll, N.; Vlasov, Y. Ultra-Low Loss Photonic Integrated Circuit with Membrane-Type Photonic Crystal Waveguides. *Opt Express* **2003**, *11* (22), 2927. <https://doi.org/10.1364/OE.11.002927>.
- (27) Marchetti, R.; Lacava, C.; Carroll, L.; Gradkowski, K.; Minzioni, P. Coupling Strategies for Silicon Photonics Integrated Chips [Invited]. *Photonics Res* **2019**, *7* (2), 201. <https://doi.org/10.1364/PRJ.7.000201>.
- (28) Zhu, Y.; Wang, J.; Xie, W.; Tian, B.; Li, Y.; Brainis, E.; Jiao, Y.; Thourhout, D. Van. Ultra-Compact Silicon Nitride Grating Coupler for Microscopy Systems. *Opt Express* **2017**, *25* (26), 33297. <https://doi.org/10.1364/OE.25.033297>.
- (29) Mak, J. C. C.; Sacher, W. D.; Ying, H.; Luo, X.; Lo, P. G.-Q.; Poon, J. K. S. Multi-Layer Silicon Nitride-on-Silicon Polarization-Independent Grating Couplers. *Opt Express* **2018**, *26* (23), 30623. <https://doi.org/10.1364/OE.26.030623>.
- (30) Son, G.; Han, S.; Park, J.; Kwon, K.; Yu, K. High-Efficiency Broadband Light Coupling between Optical Fibers and Photonic Integrated Circuits. *Nanophotonics* **2018**, *7* (12), 1845–1864. <https://doi.org/10.1515/nanoph-2018-0075>.
- (31) Mitomi, O.; Kasaya, K.; Miyazawa, H. Design of a Single-Mode Tapered Waveguide for Low-Loss Chip-to-Fiber Coupling. *IEEE J Quantum Electron* **1994**, *30* (8), 1787–1793. <https://doi.org/10.1109/3.301643>.
- (32) Zou, J.; Yu, Y.; Ye, M.; Liu, L.; Deng, S.; Xu, X.; Zhang, X. Short and Efficient Mode-Size Converter Designed by Segmented-Stepwise Method. *Opt Lett* **2014**, *39* (21), 6273. <https://doi.org/10.1364/OL.39.006273>.
- (33) Mizuno, T.; Kitoh, T.; Ishii, M.; Inoue, Y.; Saida, T.; Itoh, M.; Shibata, T.; Hibino, Y. Compact and Low-Loss Arrayed Waveguide Grating Module with Tolerance-Relaxed Spot-Size Converter. *IEEE Photonics Technology Letters* **2003**, *15* (2), 239–241. <https://doi.org/10.1109/LPT.2002.806836>.
- (34) Liu, Y.; Sun, W.; Xie, H.; Zhang, N.; Xu, K.; Yao, Y.; Xiao, S.; Song, Q. Adiabatic and Ultracompact Waveguide Tapers Based on Digital Metamaterials. *IEEE Journal of Selected Topics in Quantum Electronics* **2019**, *25* (3), 1–6. <https://doi.org/10.1109/JSTQE.2018.2846046>.
- (35) Tao, H.; Song, J.; Fang, Q.; Yu, M.; Lo, G.; Kwong, D. Improving Coupling Efficiency of Fiber-Waveguide Coupling with a Double-Tip Coupler. *Opt Express* **2008**, *16* (25), 20803. <https://doi.org/10.1364/OE.16.020803>.
- (36) Kohli, N.; Ménard, M.; Ye, W. N. Efficient TE/TM Spot-Size Converter for Broadband Coupling to Single Mode Fibers. *OSA Contin* **2019**, *2* (8), 2428. <https://doi.org/10.1364/OSAC.2.002428>.
- (37) Zhu, T.; Hu, Y.; Gatkine, P.; Veilleux, S.; Bland-Hawthorn, J.; Dagenais, M. Ultrabroadband High Coupling Efficiency Fiber-to-Waveguide Coupler Using Si₃N₄/SiO₂ Waveguides on Silicon. *IEEE Photonics J* **2016**, *8* (5), 1–12. <https://doi.org/10.1109/JPHOT.2016.2600037>.
- (38) Sethi, P.; Kallega, R.; Haldar, A.; Selvaraja, S. K. Compact Broadband Low-Loss Taper for Coupling to a Silicon Nitride Photonic Wire. *Opt Lett* **2018**, *43* (14), 3433. <https://doi.org/10.1364/OL.43.003433>.
- (39) Fernández, J.; Baños, R.; Doménech, D.; Domínguez, C.; Muñoz, P. Low-loss Inverted Taper Edge Coupler in Silicon Nitride. *IET Optoelectronics* **2019**, *13* (2), 62–66. <https://doi.org/10.1049/iet-opt.2018.5065>.

- (40) Wang, Y.; Xu, L.; Yun, H.; Ma, M.; Kumar, A.; El-Fiky, E.; Li, R.; Abadiacalvo, N.; Chrostowski, L.; Jaeger, N. A. F.; Plant, D. V. Polarization-Independent Mode-Evolution-Based Coupler for the Silicon-on-Insulator Platform. *IEEE Photonics J* **2018**, *10* (3), 1–10. <https://doi.org/10.1109/JPHOT.2018.2835767>.
- (41) Xu, L.; Wang, Y.; Kumar, A.; El-Fiky, E.; Mao, D.; Tamazin, H.; Jacques, M.; Xing, Z.; Saber, Md. G.; Plant, D. V. Compact High-Performance Adiabatic 3-DB Coupler Enabled by Subwavelength Grating Slot in the Silicon-on-Insulator Platform. *Opt Express* **2018**, *26* (23), 29873. <https://doi.org/10.1364/OE.26.029873>.
- (42) Yun, H.; Chrostowski, L.; Jaeger, N. A. F. Ultra-Broadband 2×2 Adiabatic 3 DB Coupler Using Subwavelength-Grating-Assisted Silicon-on-Insulator Strip Waveguides. *Opt Lett* **2018**, *43* (8), 1935. <https://doi.org/10.1364/OL.43.001935>.
- (43) Mao, D.; Alam, M. S.; Zhang, J.; Zhu, M.; Koh, P.-C.; Plant, D. V.; Wang, Y.; El-Fiky, E.; Xu, L.; Kumar, A.; Jaques, M.; Samani, A.; Carpentier, O.; Bernal, S. Adiabatic Coupler With Design-Intended Splitting Ratio. *Journal of Lightwave Technology* **2019**, *37* (24), 6147–6155. <https://doi.org/10.1109/JLT.2019.2946948>.
- (44) Zhu, T.; Hu, Y.; Gatkine, P.; Veilleux, S.; Bland-Hawthorn, J.; Dagenais, M. Ultrabroadband High Coupling Efficiency Fiber-to-Waveguide Coupler Using Si₃N₄/SiO₂ Waveguides on Silicon. *IEEE Photonics J* **2016**, *8* (5), 1–12. <https://doi.org/10.1109/JPHOT.2016.2600037>.
- (45) Tao, H.; Song, J.; Fang, Q.; Yu, M.; Lo, G.; Kwong, D. Improving Coupling Efficiency of Fiber-Waveguide Coupling with a Double-Tip Coupler. *Opt Express* **2008**, *16* (25), 20803. <https://doi.org/10.1364/OE.16.020803>.
- (46) Fernández, J.; Baños, R.; Doménech, D.; Domínguez, C.; Muñoz, P. Low-loss Inverted Taper Edge Coupler in Silicon Nitride. *IET Optoelectronics* **2019**, *13* (2), 62–66. <https://doi.org/10.1049/iet-opt.2018.5065>.
- (47) Bhandari, B.; Im, C.-S.; Lee, K.-P.; Kim, S.-M.; Oh, M.-C.; Lee, S.-S. Compact and Broadband Edge Coupler Based on Multi-Stage Silicon Nitride Tapers. *IEEE Photonics J* **2020**, *12* (6), 1–11. <https://doi.org/10.1109/JPHOT.2020.3036498>.
- (48) Fu, Y.; Ye, T.; Tang, W.; Chu, T. Efficient Adiabatic Silicon-on-Insulator Waveguide Taper. *Photonics Res* **2014**, *2* (3), A41. <https://doi.org/10.1364/PRJ.2.000A41>.
- (49) Pu, M.; Liu, L.; Ou, H.; Yvind, K.; Hvam, J. M. Ultra-Low-Loss Inverted Taper Coupler for Silicon-on-Insulator Ridge Waveguide. *Opt Commun* **2010**, *283* (19), 3678–3682. <https://doi.org/10.1016/j.optcom.2010.05.034>.
- (50) Hettrick, S. J.; Wang, J.; Li, C.; Wilkinson, J. S.; Shepherd, D. P. An Experimental Comparison of Linear and Parabolic Tapered Waveguide Lasers and a Demonstration of Broad-Stripe Diode Pumping. *Journal of Lightwave Technology* **2004**, *22* (3), 845–849. <https://doi.org/10.1109/JLT.2004.824548>.
- (51) Fedeli, J. M.; Orobtcchouk, R.; Seassal, C.; Vivien, L. Integration Issues of a Photonic Layer on Top of a CMOS Circuit. In *Silicon Photonics*; Kubby, J. A., Reed, G. T., Eds.; SPIE, 2006; Vol. 6125, p 61250H. <https://doi.org/10.1117/12.642672>.
- (52) Konstantinova, T. G.; Andronic, M. M.; Baklykov, D. A.; Stukalova, V. E.; Ezenkova, D. A.; Zikiy, E. V.; Bashinova, M. V.; Solovev, A. A.; Lotkov, E. S.; Ryzhikov, I. A.; Rodionov, I. A. Deep Multilevel Wet Etching of Fused Silica Glass Microstructures in BOE Solution. *Sci Rep* **2023**, *13* (1). <https://doi.org/10.1038/s41598-023-32503-w>.
- (53) Schnarrenberger, M.; Zimmermann, L.; Mitze, T.; Bruns, J.; Petermann, K. Facet Preparation of SOI Waveguides by Etching and Cleaving Compared to Dicing and Polishing. In *First IEEE International Conference on Group IV Photonics, 2004.*; 2004; pp 72–74. <https://doi.org/10.1109/GROUP4.2004.1416657>.
- (54) Buzaverov, K. A.; Baburin, A. S.; Sergeev, E. V.; Avdeev, S. S.; Lotkov, E. S.; Andronic, M.; Stukalova, V. E.; Baklykov, D. A.; Dyakonov, I. V.; Skryabin, N. N.; Saygin, M. Yu.; Kulik, S. P.; Ryzhikov, I. A.; Rodionov, I. A. Low-Loss Silicon Nitride Photonic ICs for near-Infrared Wavelength Bandwidth. *Opt. Express* **2023**, *31* (10), 16227–16242. <https://doi.org/10.1364/OE.477458>.
- (55) Baklykov, D. A.; Andronic, M.; Sorokina, O. S.; Avdeev, S. S.; Buzaverov, K. A.; Ryzhikov, I. A.; Rodionov, I. A. Self-Controlled Cleaving Method for Silicon DRIE Process Cross-Section Characterization. *Micromachines (Basel)* **2021**, *12* (5). <https://doi.org/10.3390/mi12050534>.
- (56) Hayashi, S.; Yamanaka, M.; Nakagawa, H.; Kubota, M.; Ogura, M. SiO₂ Etching Using Inductively Coupled Plasma. *Electronics and Communications in Japan (Part II: Electronics)* **1998**, *81* (9), 21–29. [https://doi.org/https://doi.org/10.1002/\(SICI\)1520-6432\(199809\)81:9<21::AID-ECJB3>3.0.CO;2-3](https://doi.org/https://doi.org/10.1002/(SICI)1520-6432(199809)81:9<21::AID-ECJB3>3.0.CO;2-3).
- (57) Oehrlein, G. S.; Zhang, Y.; Vender, D.; Haverlag, M. Fluorocarbon High-density Plasmas. I. Fluorocarbon Film Deposition and Etching Using CF₄ and

- CHF₃. *Journal of Vacuum Science & Technology A* **1994**, *12* (2), 323–332. <https://doi.org/10.1116/1.578876>.
- (58) Gaboriau, F.; Cartry, G.; Peignon, M.-C.; Cardinaud, Ch. Selective and Deep Plasma Etching of SiO₂: Comparison between Different Fluorocarbon Gases (CF₄, C₂F₆, CHF₃) Mixed with CH₄ or H₂ and Influence of the Residence Time. *Journal of Vacuum Science & Technology B: Microelectronics and Nanometer Structures Processing, Measurement, and Phenomena* **2002**, *20* (4), 1514–1521. <https://doi.org/10.1116/1.1495502>.
- (59) Kim, B.; Kwon, K.-H.; Kwon, S.-K.; Park, J.-M.; Yoo, S. W.; Park, K.-S.; You, I.-K.; Kim, B.-W. Modeling Etch Rate and Uniformity of Oxide via Etching in a CHF₃/CF₄ Plasma Using Neural Networks. *Thin Solid Films* **2003**, *426* (1), 8–15. [https://doi.org/https://doi.org/10.1016/S0040-6090\(02\)01114-8](https://doi.org/https://doi.org/10.1016/S0040-6090(02)01114-8).
- (60) He, A.; Guo, X.; Wang, T.; Su, Y. Ultracompact Fiber-to-Chip Metamaterial Edge Coupler. *ACS Photonics* **2021**, *8* (11), 3226–3233. <https://doi.org/10.1021/acsp Photonics.1c00993>.
- (61) Liao, Z.; Aitchison, J. S. Precision Etching for Multi-Level AlGaAs Waveguides. *Opt. Mater. Express* **2017**, *7* (3), 895–903. <https://doi.org/10.1364/OME.7.000895>.
- (62) Sacher, W. D.; Luo, X.; Yang, Y.; Chen, F.-D.; Loredello, T.; Mak, J. C. C.; Liu, X.; Hu, T.; Xue, T.; Guo-Qiang Lo, P.; Roukes, M. L.; Poon, J. K. S. Visible-Light Silicon Nitride Waveguide Devices and Implantable Neurophotonic Probes on Thinned 200 Mm Silicon Wafers. *Opt Express* **2019**, *27* (26), 37400. <https://doi.org/10.1364/oe.27.037400>.
- (63) Soller, B. J.; Gifford, D. K.; Wolfe, M. S.; Froggatt, M. E. High Resolution Optical Frequency Domain Reflectometry for Characterization of Components and Assemblies. *Opt. Express* **2005**, *13* (2), 666–674. <https://doi.org/10.1364/OPEX.13.000666>.
- (64) Bauters, J. F.; Heck, M. J. R.; John, D.; Dai, D.; Tien, M.-C.; Barton, J. S.; Leinse, A.; Heideman, R. G.; Blumenthal, D. J.; Bowers, J. E. Ultra-Low-Loss High-Aspect-Ratio Si₃N₄ Waveguides. *Opt. Express* **2011**, *19* (4), 3163–3174. <https://doi.org/10.1364/OE.19.003163>.
- (65) Glombitza, U.; Brinkmeyer, E. Coherent Frequency-Domain Reflectometry for Characterization of Single-Mode Integrated-Optical Waveguides. *Journal of Lightwave Technology* **1993**, *11* (8), 1377–1384. <https://doi.org/10.1109/50.254098>.